Metal-Insulator Transition in ALD VO_2 Ultrathin Films and Nanoparticles: Morphological Control

Antony P. Peter, Koen Martens, Geert Rampelberg, Michael Toeller, James M. Ablett, Johan Meersschaut, Daniel Cuypers, Alexis Franquet, Christophe Detavernier, Jean-Pascal Rueff, Marc Schaekers, Sven Van Elshocht, Malgorzata Jurczak, Christoph Adelmann, and Iuliana P. Radu*

Nanoscale morphology of vanadium dioxide (VO_2) films can be controlled to realize smooth ultrathin (<10 nm) crystalline films or nanoparticles with atomic layer deposition, opening doors to practical VO_2 metal-insulator transition (MIT) nanoelectronics. The precursor combination, the valence of V, and the density for as-deposited VO_2 films, as well as the postdeposition crystallization annealing conditions determine whether a continuous thin film or nanoparticle morphology is obtained. It is demonstrated that the films and particles possess both a structural and an electronic transition. The resistivity of ultrathin films changes by more than two orders of magnitude across the MIT, demonstrating their high quality.

1. Introduction

Vanadium dioxide (VO_2) is a material that exhibits a first order metal-insulator transition (MIT)[1] at around 67 °C, coupled with a structural transition from a low temperature monoclinic to a high temperature rutile structure. In bulk single crystals, the transition leads to a resistivity change of up to five orders of magnitude and a strong modification of optical transmission.[2] The control of electrical resistivity, infrared transmission, and strain by making use of the phase transition renders the material attractive for potential applications, such as nanoelectronic switches,[3–5] transistors,[6] optical devices,[7,8] and micromechanical devices.[9]

VO_2 thin films have been synthesized by a variety of deposition techniques, such as pulsed laser deposition (PLD),[10–14] molecular beam epitaxy (MBE),[15] reactive sputtering,[16,17] sol-gel processing,[18] chemical vapor deposition (CVD),[19] thermal oxidation,[20] and ion beam deposition.[21,22] Most of the studies report on VO_2 films with thicknesses in the range of 40–200 nm. Sub-10 nm continuous films of ≈2 nm thickness have been deposited both by PLD[23] and MBE[15] on monocrystalline TiO_2 and MITs with resistivity changes of ≈500 × and ≈25 ×, respectively. However, the use of TiO_2 monocrystals as a substrate is unfavorable for practical nanoelectronic applications and PLD and MBE are not deposition techniques that are well suited for device manufacturing. By contrast, VO_2 films deposited by techniques suitable for manufacturing, including atomic layer deposition (ALD), have typically been noncontinuous and have shown a strongly degraded MIT when the film thicknesses were below 40–50 nm.[24–26]

In recent years, ALD[27,28] has become the reference technique for the deposition of dielectric[29] and metallic[30] thin films for nanoelectronic applications.[31–33] ALD is characterized by self-limiting surface reactions, which enables a precise control over film thickness and stoichiometry. In addition, the high conformality allows deposition onto three-dimensional (3D) structures, as increasingly required for advanced nanoelectronic applications. However, the ALD growth of thin high quality VO_2 is not established yet. VO_2 ALD has been reported using vanadyl acetonate and O_2[34] or $VOCl_3$.[35] X-ray diffraction (XRD) indicated the presence of VO_2 and signs of MITs have been observed. Yet, these processes have not been able to achieve thin, continuous, and phase-pure films. By contrast, the ALD from tetrakis(ethylmethylamino) vanadium (TEMAV) and O_3 has led to continuous smooth films that show an MIT down to a thickness of ≈40 nm.[36–39] ALD VO_2 from TEMAV with H_2O as oxygen source has been reported to lead to mixed valence VO_x films which can be converted to VO_2 by postannealing.[40] Nevertheless, no continuous ALD VO_2 films featuring an MIT

Dr. A. P. Peter, Dr. K. Martens, Dr. M. Toeller, Dr. J. Meersschaut, Dr. D. Cuypers, Dr. A. Franquet, Dr. M. Schaekers, Dr. S. V. Elshocht, Dr. M. Jurczak, Dr. C. Adelmann, Dr. I. P. Radu
Imec, B-3001, Leuven, Belgium
E-mail: koen.martens@imec.be
Dr. K. Martens
Department of Electrical Engineering (ESAT)
KU Leuven, B-3001, Leuven, Belgium
G. Rampelberg, Prof. C. Detavernier
Department of Solid State Science
CoCooN, Universiteit Gent
B-9000, Gent, Belgium
Dr. M. Toeller
Tokyo Electron America, Inc.
Austin, Texas 78741, USA
Dr. J. M. Ablett, Dr. J.-P. Rueff
Synchrotron SOLEIL
91192, Gif-sur-Yvette, France

DOI: 10.1002/adfm.201402687

with thicknesses below 40 nm have been reported thus far. To unlock the full potential of VO_2 for scaled nanoelectronic applications, it is however necessary to demonstrate VO_2 films with both a large resistance change during the MIT as well as thicknesses below 10 nm. In addition, these films need to be deposited on technologically relevant Si substrates by a manufacturing friendly technique, such as ALD.

Nonplanar crystalline VO_2 nanostructures are also of fundamental and applied interest. In previous work, polycrystalline VO_2 nanorods have been synthesized using a hydrothermal process.[41–43] These rods had average diameters of 20–40 nm and lengths of 1–5 μm. Another hydrothermal protocol yielded anisotropic free-standing single-crystal VO_2 nanowires with diameters of 58–200 nm and lengths greater than 10 μm.[44] Single crystalline, well-faceted VO_2 nanowires synthesized using a vapor transport method are reported in.[45] Their diameters were 60 ± 30 nm and their lengths could reach 10 μm and above.[46,47] VO_2 nanoparticles with controlled size were reported to be produced by coimplantation of vanadium and oxygen into an amorphous SiO_2 matrix followed by a thermal anneal of 1000 °C. The equivalent radius of these particles varied between 40–90 nm.[48] Another route for VO_2 nanoparticle synthesis consisted of depositing substoichiometric films by PLD followed by an anneal.[49,50] Most nanostructures thus reported feature dimensions of 40–100 nm and above.

In this work, we demonstrate continuous sub-10 nm thick ALD VO_2 films which exhibit both structural and electronic MITs. These films show a change in sheet resistivity of more than two orders of magnitude across the phase transition. To obtain such films, a tight control of the deposition and annealing conditions of VO_2 is the key. The density and stoichiometry changes during film formation were anticipated to play a crucial role in morphological control. We have indeed found that as deposited densities and stoichiometries closer to those of VO_2 allowed the formation of closed smooth films. Moreover, we show that film morphology can be tuned by the process parameters allowing to either obtain smooth films or nanoparticles (down to ≈20-nm-size), which all show an MIT.

2. Results

The ALD was carried out using tetrakis[ethylmethylamino] vanadium [$V(NEtMe)_4$, TEMAV, provided by Air Liquide]. A central issue for the deposition of VO_2 films, both by ALD and other deposition methods, is the control of the oxidation state of V. V can exist in all oxidation states between +2 and +5. As a result, a myriad of stable vanadium oxide phases other than VO_2, including VO, V_2O_3, V_3O_5, V_4O_7, V_6O_{13}, and V_2O_5, have been observed. In TEMAV, V is already present in the desired V^{4+} oxidation state, which may facilitate the direct formation of VO_2 during ALD.[37] Furthermore, the choice of the oxidizer is important to obtain uniform, conformal, and high quality ALD films of the desired phase with the right V valence.[51,52] Previous work using O_3 as oxidizer led to the formation of V^{5+} in the as-deposited films, which required subsequent annealing under reducing conditions to obtain VO_2.[38]

In this work, we study the ALD using TEMAV in combination with H_2O as oxidizer. All films were deposited at 150 °C on 300 mm Si (100) substrates in a Tokyo Electron EX reactor. Prior to ALD, either 1 nm of SiO_2 (by rapid thermal oxidation) or 18 nm of crystalline Al_2O_3 were grown. Al_2O_3 was deposited by ALD from $Al(CH_3)_3$ and H_2O at 300 °C followed by annealing at 1000 °C in N_2 to crystallize the films into the γ-Al_2O_3 phase with (111) fiber texture. All data below correspond to VO_2 on Al_2O_3 unless noted otherwise. The ALD growth of this process is linear and the growth rate is 0.05 nm $cycle^{-1}$, as determined by ellipsometry.

The as-deposited vanadium oxide films were amorphous, as determined by grazing incidence XRD (GIXRD, $\omega = 1°$, CuKα). Hard X-ray photoelectron spectroscopy (HAXPES, measured at the GALAXIES beamline at SOLEIL[53] spectra for 30 nm as-deposited vanadium oxide (**Figure 1**a) are consistent with V present in the film as V^{4+}. Both the binding energy difference between the O 1s and V $2p_{3/2}$ peaks,[54,55] and in particular the observation of filled V 3d states in the valence band close to the Fermi level (Figure 1b) are strong indicators of V^{4+}. Note that the latter observation rules out V^{5+} as the main oxidation state since V^{5+} has a $3d^0$ configuration. The observation of V^{4+} in as-deposited films is in contrast to the O_3-based ALD process using the same precursor where V was present as V^{5+}.[38] The direct formation of V^{4+} in the H_2O-based ALD process can be explained by the much lower oxidizing strength of H_2O with respect to O_3. Furthermore, H_2O reacts with the TEMA (tetrakis[ethylmethylamino]) ligands of TEMAV by proton transfer and subsequent release of the hydrogenated ligand.[56] It is very plausible that the overall ALD surface reaction chemistry leaves the oxidation state of the V cation intact. Hence, the V^{4+} in the TEMAV precursor can be successfully transferred to V^{4+} in the deposited film. This demonstrates that ALD is capable of depositing suboxides using H_2O as the oxidizer when the metal cation in the precursor already has the desired oxidation state.

The as-deposited amorphous VO_2 films showed no electronic MIT as observed by sheet resistivity measurements (not shown). Hence, a postdeposition anneal (PDA) was necessary to crystallize the films. To avoid oxidation or reduction of the films, an N_2/O_2 ambient was used and the partial O_2 pressure during anneal was carefully adjusted to maintain the stoichiometry of the VO_2 films.

The GIXRD pattern of an 8-nm-thick VO_2 film (Figure 1e) shows that the film crystallized in the monoclinic VO_2(M) phase after an optimized PDA (see below) at 480 °C and a O_2 partial pressure of 1.6 Pa. The peak at $2\theta = 27.8°$ corresponds to the (011) diffraction planes of VO_2 (M). The VO_2(M) phase was found by GIXRD for the entire investigated thickness range of 4–30 nm without any signatures of secondary phases. Further evidence for the presence of vanadium in the +4 oxidation state after PDA comes from the HAXPES spectra (Figure 1a). The V 2p HAXPES spectrum shows only negligible shift upon annealing. Note that the peculiar shape of the V $2p_{3/2}$ peak can be attributed to multiplet effects due to interactions of the 2p core hole with the partly-filled 3d states[57] rather than the presence of multiple oxidation states. The absence of the multiplet structure in the amorphous as-deposited film may be due to disorder effects which lead to locally different V coordination. Furthermore, the observation of filled V 3d states close to the Fermi level in the valence

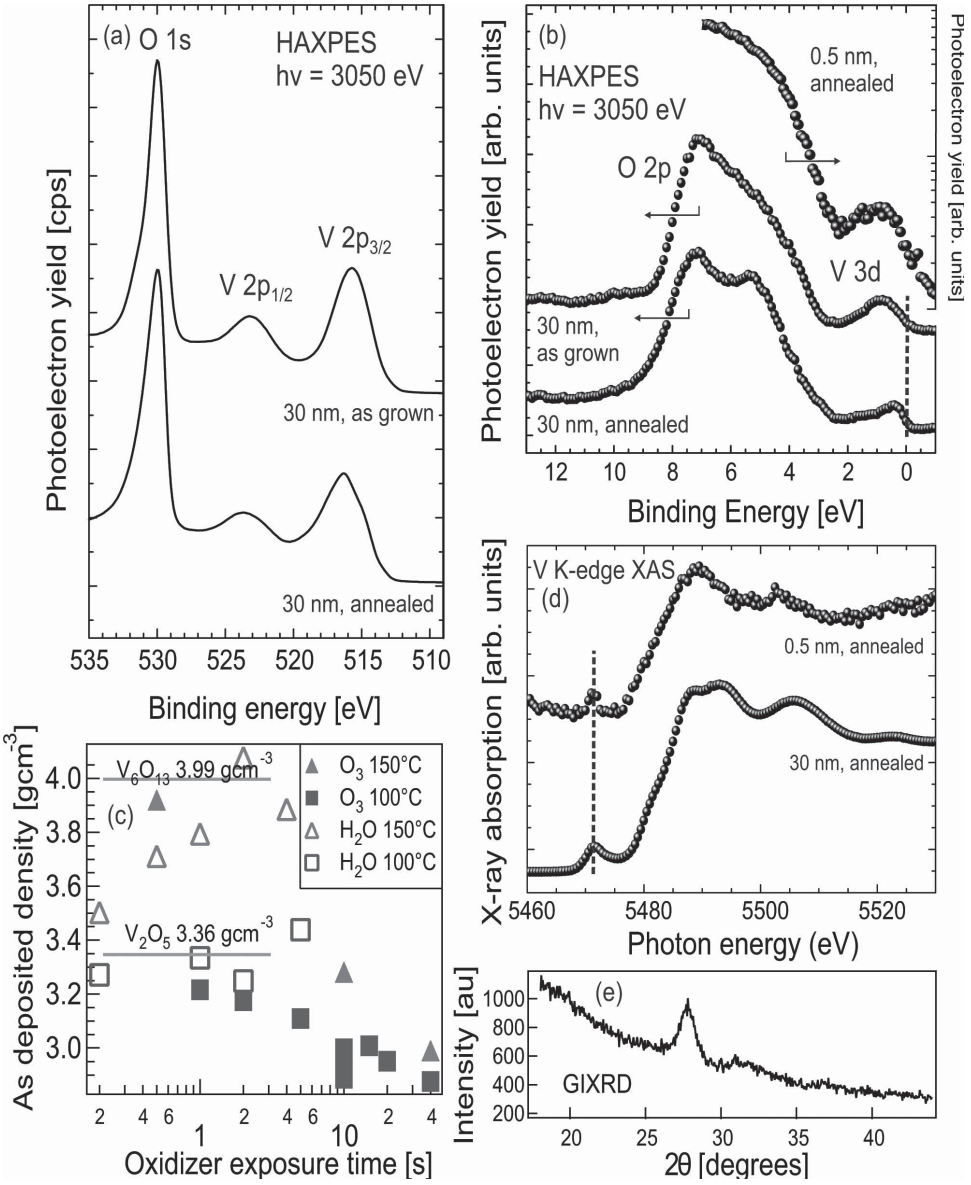

Figure 1. a) V 2p and O 1s HAXPES spectra for as-deposited and annealed H_2O-based ALD VO_2 films. The spectra are consistent with V in the +4 oxidation state. b) The valence band HAXPES spectra show the presence of filled 3d states close to the Fermi level as expected for $3d^1$ VO_2. c) As-deposited film density as determined by film mass measurements and volume derived from ellipsometry for different oxidizers and temperatures. The H_2O process at 150 °C led to the highest film density. For comparison, the bulk VO_2 density is 4.6 g cm^{-3}. d) V K-edge XAS spectra of 0.5- and 30-nm-thick annealed VO_2 films. e) GIXRD with $2\theta = 27.8°$ (011) diffraction peak showing the VO_2(M1) crystalline structure for 8-nm-thick films after crystallization by PDA.

band spectrum (Figure 1b) after annealing indicates the presence of V^{4+} also in the annealed films and rules out the dominance of V^{5+}.

The presence of V^{4+} is also corroborated by the V K-edge X-ray absorption spectroscopy (XAS), measured by total-photoelectron yield at the GALAXIES beamline at SOLEIL) spectra in Figure 1d. Both the position and the shape of the preedge peak as well as the energies of characteristic features at and above the absorption edge in the direct and derivative (not shown) spectra are consistent with V^{4+}.[58,59] Note that the position and the shape of the preedge peak does remain constant even for ultrathin noncontinuous nanocluster structures down to a nominal thickness of 0.5 nm. The valence band HAXPES spectrum (Figure 1b) shows the V_{4+} stoichiometry in the 0.5-nm films as well. This indicates that the deposition and annealing processes discussed here are capable of obtaining V^{4+} in thin films irrespective of the film thickness down to values even in the sub-nm range.

Postdeposition crystallization annealing, especially in the case when a valence change is necessary to obtain stoichiometric VO_2, is typically accompanied by rough morphology and agglomeration on dielectric substrates. As an example, noncontinuous and rough VO_2 films were obtained using TEMAV and O_3 even for optimized annealing conditions.[38]

The agglomeration and the film roughening can be linked to dewetting of the dielectric surfaces by the metallic VO_2 and is strongly enhanced by the volume change during the crystallization anneal. Hence, continuous and smooth thin films are favored when VO_2 is deposited not only in the right stoichiometry but also with a density approaching that of the VO_2 as close as possible.

Figure 1c illustrates the dependence of the density of as-deposited VO_2 on the oxidizer (O_3 vs H_2O) and the deposition temperature. The density was deduced from the mass increase of the wafer due to VO_2 deposition in combination with the film thickness determined by ellipsometry. The use of H_2O at 150 °C led to the highest density closest to VO_2. Low temperature and strongly oxidizing O_3 conditions led to much lower densities due to V_2O_5 formation and/or C contamination (not shown). As demonstrated below, the combination of V^{4+} and high density in the as-deposited films that was realized using H_2O at 150 °C is an enabling condition for smooth and continuous ultrathin VO_2 films with thicknesses below 10 nm.

The morphology of the films as a function of their thickness was investigated by scanning electron microscopy (SEM) and atomic-force microscopy (AFM) (**Figure 2**a–c). Here, the PDA was carried out at 500 °C in 1.6 Pa O_2 partial pressure. The films were found to be uniform, with no agglomeration observed down to a thickness of 8 nm. For a thickness of 4 nm, the SEM image suggested that the film was noncontinuous. The rms roughness, as determined by AFM was in the range of 2.5 nm for all samples and thus rather independent of the film thickness. It should be noted however that the measured rms roughness of 2.7 nm for the 4-nm-thick film was comparable to the film thickness, corroborating the noncontinuous grain-like morphology of the film, as observed by SEM.

The VO_2 film closure as a function of thickness was measured by time-of-flight secondary ion mass spectrometry (TOF-SIMS). Figure 2e shows ToF-SIMS surface Al^+ secondary ion yield (left axis) measured as a function of vanadium area density determined by Rutherford backscattering spectroscopy (RBS). The strong decrease of the Al^+ surface yield indicates an increasing coverage of the Al_2O_3 surface by VO_2. At V area densities corresponding to a VO_2 thickness of 8 nm and above, the Al^+ yield saturated at a background level of a few percent, indicating that the VO_2 layers are essentially closed and fully cover the surface.

A cross-sectional transmission electron microscope (TEM) micrograph of the 8-nm-thick VO_2 films after PDA is shown in Figure 2d. The micrograph, in combination with high-angle annular dark-field scanning transmission electron microcopy analysis (not shown), indicated that the film was uniform and that the interface of VO_2 with Al_2O_3 was sharp and regular. No voids or interdiffusion of Al_2O_3 and VO_2 were observed.

The impact of the film morphology and the thickness on the electrical resistivity of VO_2, in particular across the MIT, is shown in Figure 2f. Generally, the magnitude of the resistivity change across the MIT decreased with decreasing film thickness, whereas the resistivity increases. The thickness dependence was however rather weak down to a film thickness of 14 nm and strong variations were only observed for the thinnest, 4-nm-thin, film. This can be related to an increased impact of film roughness as the film thickness decreases, and in particular to the increasing loss of film continuity when the thickness approaches 4 nm. Nonetheless, even in this case, signs of a MIT are visible in the data although the transition magnitude was strongly reduced. This highlights the importance of the

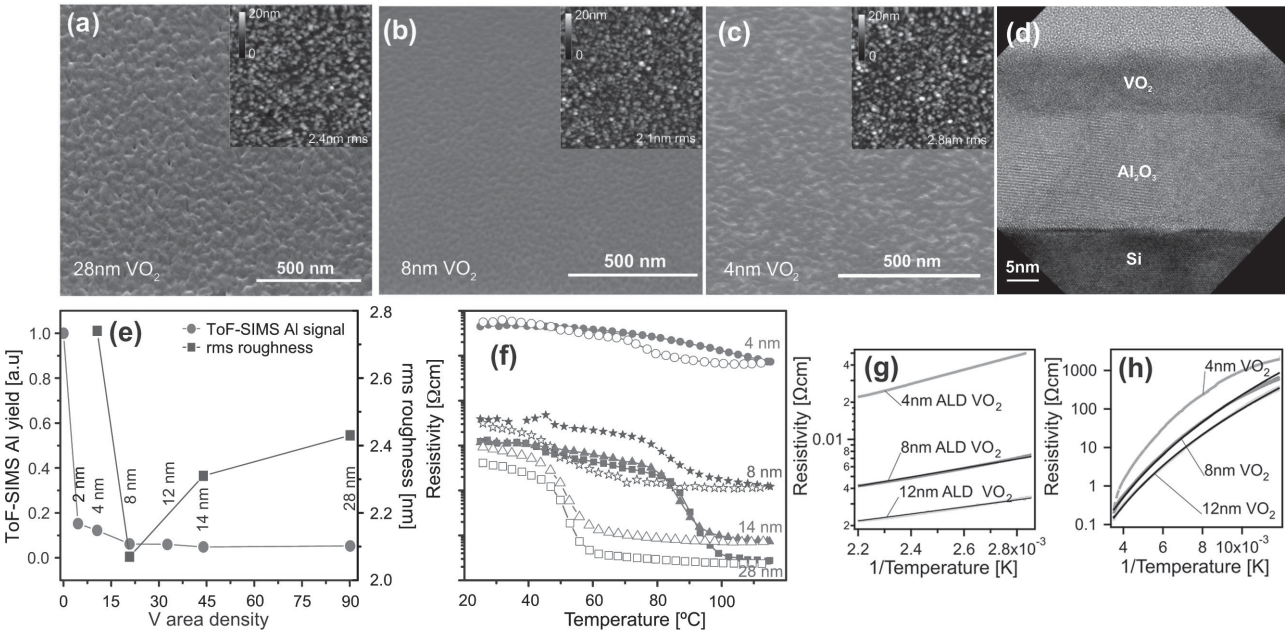

Figure 2. a–c) Top-view SEM and 1 × 1 μm² AFM images of VO_2 films after PDA with thicknesses as indicated; d) Cross-sectional TEM micrograph of a 8 nm VO_2 film after PDA; e) ToF-SIMS Al^+ yield and AFM rms roughness as a function of RBS V area density. The nominal VO_2 film thickness is also indicated. The onset of film closure can be observed at ≈8 nm; g–h) Resistivity as a function of temperature below (semiconducting, 80–280 K); g) and above (metallic, 350–474 K); h) the MIT temperature.

film morphology and continuity for the observation of large-magnitude MITs in ultrathin VO_2 films.

The temperature dependence of the resistivity and the impact of the morphology below and above the MIT were also investigated. Below the transition temperature (i.e., in the semiconducting phase), no Arrhenius behavior of the resistivity was observed (see Figure 2h). By contrast, within the 80–280 K temperature range, the temperature dependence for the 12-nm-thick film shows behavior similar to 3D Mott variable range hopping ($\rho = \rho_0 \exp\left(\left(\frac{T_0}{T}\right)^{1/4}\right)$).[60] Variable range hopping fits are shown as black lines in Figure 2h). For lower film thicknesses, the temperature dependence deviates from that observed for thicker films, especially at the lowest temperatures. The deviations coincide with the increased influence of roughness and film noncontinuity. In the metallic phase (Figure 2g), for thicknesses of 8 and 12 nm, the temperature dependence was most consistent with Schottky emission ($\sigma \approx T^2 \exp(-E_a/kT)$) across grain boundaries. For the lowest thickness (4 nm), the data were best accounted for by a pure Arrhenius dependence. This behavior was found[61] to be characteristic for ultrathin islanded metal films, which is consistent with our observed film morphology.

As discussed above, the morphology of the resulting VO_2 nanostructures can be controlled by as-deposited density and annealing conditions. In the above section, the deposition and in particular, the annealing conditions were optimized to obtain smooth and continuous films even for thicknesses <10 nm. However, the morphology control can also be exploited to obtain VO_2 nanoclusters by raising the annealing temperature. For VO_2 films with nominal thicknesses of 4 and 6 nm, a PDA at 540 °C in 1.6 Pa O_2 resulted in the formation of nanoparticles. SEM and AFM images of these nanoclusters are shown in **Figure 3**a,b,e,f. The particle size increased with the amount of deposited material. Using XRD, the average particle size was derived from the width of the (011) peak width using a Scherrer analysis. Average VO_2 nanocluster diameters of 15 and 18 nm were obtained for nominally 4- and 6-nm-thick films, respectively, in agreement with SEM and AFM observations. As expected for such isolated nanostructures, it was not possible to measure a finite sheet resistance. However, these VO_2 nanoclusters showed both a structural and electronic transition with temperature that was consistent with the MIT (see Figure 3, c,d,g,h). The ellipsometry amplitude ratio (Ψ) measured as a function of temperature showed the presence of an optical/electronic transition in the same temperature range as expected for the VO_2 MIT. Furthermore, temperature-dependent XRD confirmed a structural transition in the same temperature range. This demonstrates that it is possible to obtain both 2D (smooth film) and 0D (nanoparticle) VO_2 nanostructure morphologies with ALD simply by adapting the PDA temperature.

We now discuss in detail the properties of thin VO_2 films at the transition and the optimization of the magnitude of the resistivity change across the MIT. In situ XRD measurements[37] as a function of temperature showed the presence of a reversible structural phase transition across the MIT for a 30-nm-thick film annealed at 500 °C in 1.6 Pa O_2 (see **Figure 4**a,b). A peak shift of ≈0.10–0.15° was observed around 70 °C reversing to the original position when cooled. The change of the 2θ peak position from a ≈28.0° (011) VO_2(M1) peak around 68 °C (during heating) to a lower angle 2θ = 27.75° (110) VO_2(R) peak (and vice-versa) was due to the phase change from the monoclinic VO_2(M1) phase to the tetragonal VO_2(R) phase at the MIT. The structural transition, including the hysteresis characteristic for the VO_2 first order MIT, was still visible for the 8-nm film (Figure 4e). Figure 4d shows the optical characteristics as observed by ellipsometry at a wavelength of 1000 nm. The ellipsometry amplitude ratio (Ψ) showed the presence of a concomitant optical/electronic transition in the VO_2 films that accompanied the electrical MIT deduced from resistivity measurements.

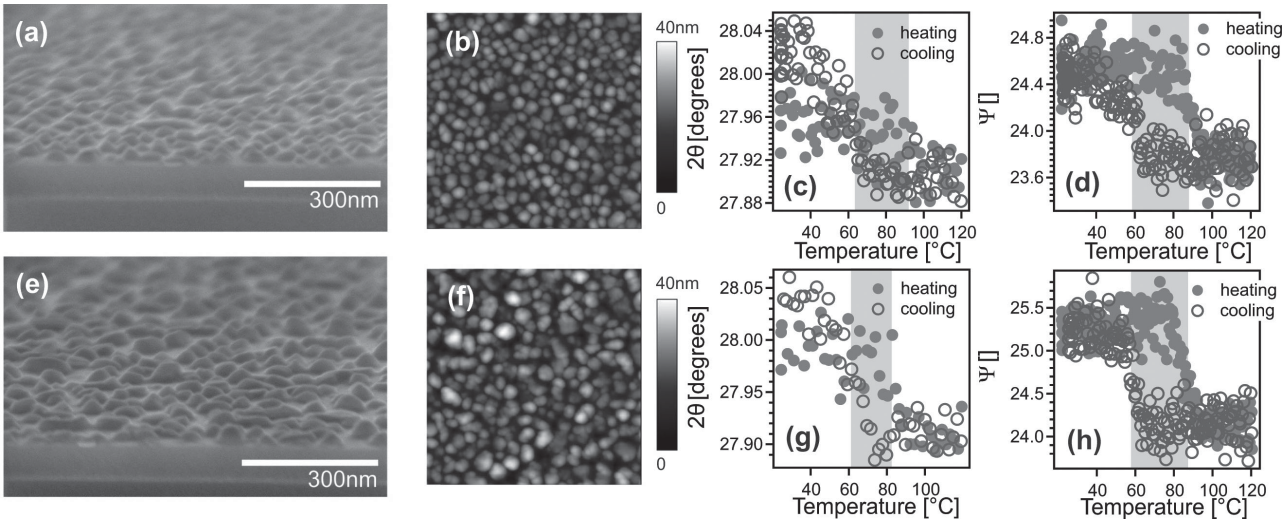

Figure 3. SEM images of nanoparticles obtained by annealing of nominally; a) 4-nm- and; e) 6-nm-thick VO_2 films on SiO_2 at 540 °C. b) and f) show 1×1 μm^2 AFM images of the same samples respectively. The variation of the 2θ position of the main peak in the XRD pattern with temperature indicates a structural transition from monoclinic VO_2(M1) to tetragonal VO_2(R) for the nanoclusters derived from nominally c) 4 and g) 6 nm VO_2. The ellipsometry amplitude ratio Ψ shows the presence of a concomitant optical/electronic transition for the nominally 4 d) and 6 nm h) nanoclusters.

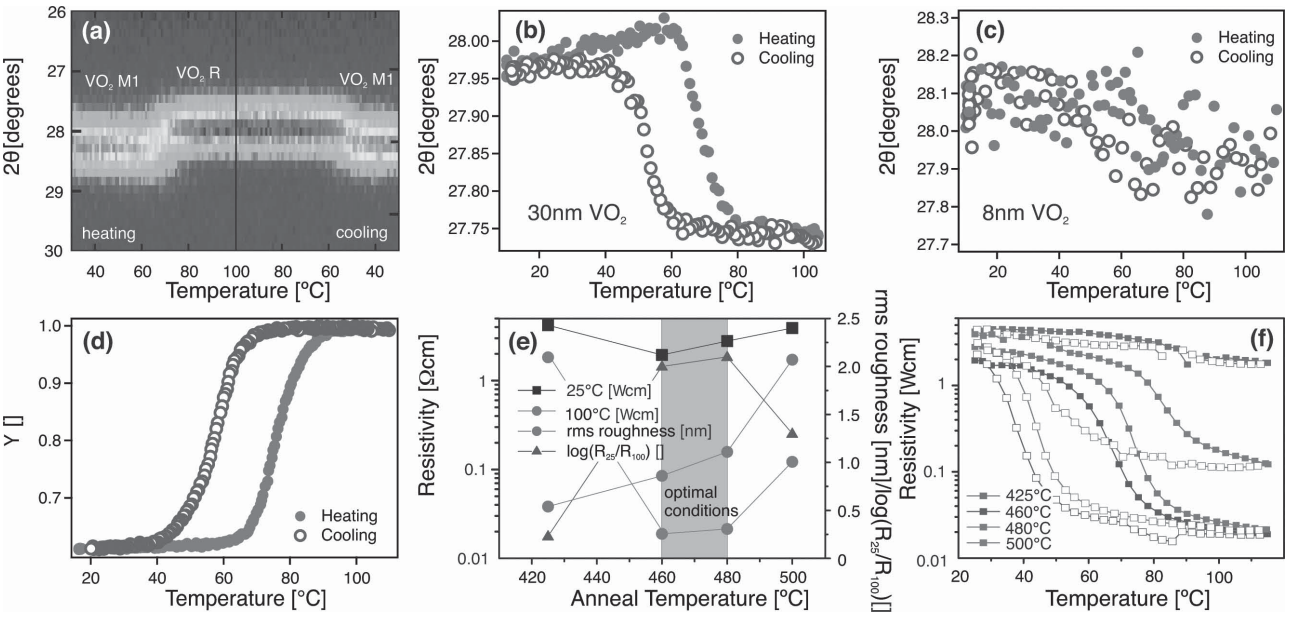

Figure 4. a) Temperature dependent 2θ-ω XRD pattern of a 28-nm-thick VO_2 film across the MIT (temperature range 30–100 °C); b) XRD peak position as a function of temperature for the same film; c) Temperature-dependent XRD peak position obtained by Gaussian peak fitting of an 8 nm ALD VO_2 film. d) Ellipsometry amplitude ratio (Ψ) at $\lambda = 1000$ nm as a function of temperature. e) Resistivity in the semiconducting and metallic states for films with various anneal temperatures extracted from f) (left ordinate). AFM rms film roughness and magnitude of transition versus anneal temperature (right ordinate). The region exhibiting the highest magnitude of transition is shaded. f) Resistivity curves across the MIT for 8 nm VO_2 films annealed at different temperatures with fixed O_2 partial pressure of 1.6 Pa.

The magnitude of the electronic MIT of 8-nm-thick VO_2 films could be optimized by tuning the PDA at a fixed oxygen partial pressure of 1.6 Pa. For optimized PDA temperatures of 460–480 °C, the resistivity change across the transition (defined as the ratio of the resistivity at 25 and 100 °C, respectively; ρ_{25}/ρ_{100}) for the 8-nm film reached more than two orders of magnitude, as shown in Figure 4e,f. Films annealed at 425 °C show practically no transition, while increasing the anneal temperature to 500 °C, decreases the ratio to ≈10. The morphology of the films was investigated by AFM (Figure 4e). Films annealed at 425 °C, although smooth with a low rms roughness of 0.5 nm, showed a poor transition magnitude likely due to lack of film crystallinity. The crystalline films, annealed at 460 and 480 °C, showed an rms roughness of 0.9–1.1 nm and a resistivity change of more than two orders of magnitude across the MIT. By contrast, a PDA at 500 °C result in rougher films with an rms roughness of 2.1 nm, coinciding with a deterioration in the magnitude of the transition.

3. Conclusions

In conclusion, we have shown how an increased morphological control can be used to obtain smooth and continuous VO_2 films with thicknesses below 10 nm. Key parameters are the choice of precursor, oxidizer, and PDA conditions ensuring that dense films with the right V valence state can be directly achieved by the deposition process and maintained during crystallization annealing. This was realized by an ALD process using TEMAV in combination with H_2O. Such films showed a large MIT with a resistivity change of over two magnitudes for films as thin as 8 nm. For the thinnest films, the magnitude of the resistance change across the MIT decreased because of the formation of isolated nanoparticles rather than continuous films. However, the data indicated that no intrinsic thickness limits existed for the deposition of crystalline VO_2 nanostructures with an MIT by this process. The resulting VO_2 nanoparticles with diameters of 10–20 nm, all showed both electronic and structural phase transitions in the same temperature range as the thin films.

4. Experimental Section

ALD was carried out using TEMAV precursor in combination with H_2O as oxidizer. All films were deposited at 150 °C on 300 mm Si (100) substrates in a Tokyo Electron EX reactor. Prior to ALD, either 1 nm of SiO_2 (by rapid thermal oxidation) or 18 nm of crystalline Al_2O_3 were grown. Al_2O_3 was deposited by ALD from $Al(CH_3)_3$ and H_2O at 300 °C followed by annealing at 1000 °C in N_2 to crystallize the films into the γ-Al_2O_3 phase with (111) fiber texture.

Layer thickness was measured by 49-point spectroscopic ellipsometry (SE) and X-ray reflectivity. SE was carried out in a KLATencor Aleris system. Dual harmonic oscillator models were employed to determine the thickness. The crystallinity of the films was determined by grazing incidence X-ray diffraction (GIXRD, ω = 1°) using Cu Kα radiation in a Bede Metrix-L X-ray diffractometer. In situ XRD was carried out with a heating/cooling rate and collection time of 0.1 °C s^{-1} and 10 s in inert He ambience. The roughness of the films was imaged using atomic-force microscopy (AFM) in tapping mode (Model Nanoscope dimension 3100) with an etched single crystal silicon probe tip having a radius curvature <10 nm. SEM morphology analysis was carried out using a Hitachi SU8000 system. Vanadium concentration measurements were performed by Rutherford back scattering (RBS) analysis using a 1.5 MeV He^+ beam with a scattering angle of 170°. The VO_2 film closure was measured by TOF-SIMS using an ION–TOF–IV

instrument with a Bi^{3+} source operating at a beam energy of 25 keV (area of 250 μm × 250 μm for analysis) and a Xe^{+} beam with an energy of 350 eV. TEM measurements were recorded with a FEI Tecnai F30 electron microscope operating at 300 kV, after focused ion beam sample preparation. CVD glass and Al layers were applied for better contrast. Sheet resistance was measured using a 4-point probe technique in a heated sample stage. Hard X-ray photoelectron spectroscopy (HAXPES) was measured at the GALAXIES beamline at SOLEIL.[53] V K-edge X-ray absorption spectroscopy (XAS) was measured by total-photoelectron yield at the GALAXIES beamline at SOLEIL as well.

Acknowledgment

This work was supported by the imec Industrial Affiliate Program and the TEL–imec joint development program on RRAM materials. I.P.R. and K.M. acknowledge financial support through an FWO fellowship and a Marie Curie Reintegration Grant. The authors thank Nico Jossart for the SEM analysis. The authors acknowledge SOLEIL for provision of synchrotron radiation facilities and the staff at the GALAXIES beamline for help during the experiment.

Received: August 7, 2014
Revised: November 14, 2014
Published online: December 15, 2014

[1] F. J. Morin, *Phys. Rev. Lett.* **1959**, *3*, 34.
[2] J. Nag, R. F. Haglund Jr., *J. Phys.: Condensed Matter* **2008**, *20*, 264016.
[3] M.-J. Lee, Y. Park, D.-S. Suh, E.-H. Lee, B. Park, *Adv. Mater.* **2007**, *19*, 3919.
[4] C.-R. Cho, S. Cho, S. Vadim, R. Jung, I. Yoo, *Thin Solid Films* **2006**, *495*, 375.
[5] K. Martens, I. Radu, S. Mertens, X. Shi, L. Nyns, S. Cosemans, P. Favia, H. Bender, T. Conard, M. Schaekers, S. D. Gendt, V. Afanas'ev, J. Kittl, M. Heyns, Jurczak, *J. Appl. Phys.* **2012**, *112*, 124501.
[6] J. Jeong, N. Aetukuri, T. Graf, T. D. Schladt, M. G. Samant, S. S. P. Parkin, *Science* **2013**, *339*, 1402.
[7] S. Chen, H. Ma, X. Yi, H. Wang, X. Tao, *Infrared Phys. Technol.* **2004**, *45*, 239.
[8] K. Appavoo, B. Wang, N. F. Brady, M. Seo, J. Nag, R. P. Prasankumar, D. J. Hilton, S. T. Pantelides, R. F. Haglund, *Nano Lett.* **2014**, *14*, 3.
[9] K. Liu, C. Cheng, J. Suh, Tang-R. Kong, D. Fu, S. Lee, J. Zhou, L. Chua, J. Wu, *Adv. Mater.* **2013**, *26*, 1746.
[10] Y. Muraoka, Z. Hiroi, *Appl. Phys. Lett.* **2002**, *80*, 583.
[11] K. Nagashima, T. Yanagida, H. Tanaka, H. Kawai, *J. Appl. Phys.* **2006**, *100*, 063714.
[12] J. Nag, E. Payzant, K. More, J. Haglund, *Appl. Phys. Lett.* **2011**, *98*, 251916.
[13] J. Narayan, V. Bhosle, *J. Appl. Phys.* **2006**, *100*, 103524.
[14] H. Zhou, M. Chisholm, T. Yang, S. Pennycook, J. Narayan, *J. Appl. Phys.* **2011**, *110*, 073515.
[15] N. Quackenbush, J. Tashman, J. Mundy, S. Sallis, H. Paik, R. Misra, J. Moyer, J. Guo, D. Fischer, J. Woicik, D. Muller, D. Schlom, L. Piper, *Nano Lett.* **2013**, *13*, 4857.
[16] C. Ko, Z. Yang, S. Ramanathan, *ACS Appl. Mater. Interfaces* **2011**, *3*, 3396.
[17] Y. Shigesato, M. Enomoto, H. Odaka, *Jpn. J. Appl. Phys.* **2000**, *39*, 6016.
[18] B. Chae, H. Kim, S. Yun, *Electrochem. Solid-State Lett.* **2008**, *11*, D53.
[19] M. Sahana, M. Dharmaprakash, S. Shivashankar, *J. Mater. Chem.* **2002**, *12*, 333.
[20] I. Radu, K. Martens, S. Mertens, C. Adelmann, X. Shi, H. Tielens, M. Schaekers, G. Pourtois, S. V. Elshocht, S. D. Gendt, M. Heyns, J. Kittl, *ECS Trans.* **2011**, *35*, 233.
[21] J. Natale, P. Hood, A. Harker, *J. Appl. Phys.* **1989**, *66*, 5844.
[22] K. West, J. Lu, J. Yu, D. Kirkwood, W. Chen, Y. Pei, J. Claassen, S. Wolf, *J. Vac. Sci. Technol. A* **2008**, *26*, 133.
[23] K. Martens, N. Aetukuri, J. Jeong, M. Samant, S. Parkin, *Appl. Phys. Lett.* **2014**, *104*, 081918.
[24] G. Xu, P. Jin, M. Tazawa, K. Yoshimura, *Appl. Surf. Sci.* **2005**, *244*, 499.
[25] D. Brassard, S. Fourmaux, M. Jacques, J. Kieffer, M. E. Khakani, *Appl. Phys. Lett.* **2005**, *87*, 051910.
[26] J. Suh, R. Lopez, L. Feldman, R. Haglund, *J. Appl. Phys.* **2004**, *96*, 1209.
[27] S. M. George, *Chem. Rev.* **2010**, *110*, 111.
[28] R. L. Puurunen, *J. Appl. Phys.* **2005**, *97*, 121301.
[29] M. Ritala, K. Kukli, A. Rahtu, P. I. Raisanen, M. Leskela, T. Sajavaara, J. Keinonen, *Science* **2000**, *288*, 319.
[30] B. S. Lim, A. Rahtu, R. G. Gordon, *Nat. Mater.* **2003**, *2*, 749.
[31] R. Chau, B. Doyle, S. Datta, J. Kavalieros, K. Zhang, *Nat. Mater.* **2007**, *6*, 810.
[32] D. H. Kwon, K. M. Kim, J. H. Jang, J. M. Jeon, M. H. Lee, G. H. Kim, X. Shu, G. S. Park, B. Lee, M. K. Han, C. S. Hwang, *Nat. Nanotechnol.* **2010**, *5*, 148.
[33] A. Javey, H. Kim, M. Brink, Q. Wang, A. Ural, J. Guo, P. McIntyre, P. McEuen, M. Lundstorm, H. Dai, *Nat. Mater.* **2002**, *1*, 241.
[34] P. Dagur, A. Mane, S. Shivashankar, *J. Cryst. Growth* **2005**, *275*, 1223.
[35] I. Povey, M. Bardosova, F. Chalvet, M. Pemble, H. Yates, *Surf. Sci. Coatings* **2007**, *201*, 9345.
[36] G. Rampelberg, M. Schaekers, K. Martens, Q. Xie, D. Deduytsche, B. D. Schutter, N. Blasco, J. Kittl, C. Detavernier, *Appl. Phys. Lett.* **2011**, *98*, 162902.
[37] G. Rampelberg, D. Deduytsche, B. D. Schutter, P. Premkumar, M. Toeller, M. Schaekers, K. Martens, I. Radu, C. Detavernier, *Thin Solid Films* **2014**, *550*, 59.
[38] P. Premkumar, M. Toeller, I. Radu, C. Adelmann, M. Schaekers, J. Meersschaut, T. Conard, S. V. Elshocht, *ECS J. Solid State Sci. Technol.* **2012**, *1*, 169.
[39] T. Madhavi, K. Zhang, D. Nminibapiel, V. Pallem, C. Dussarrat, W. Cao, T. Adam, C. Johnson, H. Elsayed-Ali, H. Baumgart, *ECS J. Solid State Sci. Technol.* **2014**, *3*, N89.
[40] T. Blanquart, J. Niinisto, M. Gavagni, V. Longo, M. Heikkila, E. Puukilainen, V. R. Pallem, C. Dussarrat, *RSC Adv.* **2013**, *3*, 1179.
[41] G. R. Patzke, F. Krumeich, R. Nesper, *Angew. Chem Int. Ed.* **2002**, *41*, 2446.
[42] Z. Gui, R. Gan, W. Mo, X. Chen, L. Yang, S. Zhang, Y. Hu, Z. Wang, W. Fan, *Chem. Mater.* **2002**, *14*, 5053.
[43] L. Q. Mai, W. Chen, Q. Xu, J. F. Peng, Q. Y. Zhu, *Int. J. Nanosci.* **2003**, *3*, 225.
[44] L. Whittaker, C. Jaye, Z. Fu, D. A. Fischer, S. Banerjee, *J. Am. Chem. Soc.* **2009**, *131*, 8884.
[45] B. S. Guiton, Q. Gu, A. L. Prieto, M. S. Gudiksen, H. Park, *J. Am. Chem. Soc.* **2005**, *127*, 498.
[46] J. Wei, Z. Wang, W. Chen, D. Cobden, *Nat. Nanotechnol.* **2009**, *4*, 420.
[47] J. Wu, Q. Gu, B. Guiton, N. P. de Leon, L. Ouyang, H. Park, *Nano Lett.* **2006**, *6*, 2313.
[48] R. Lopez, L. Boatner, T. Haynes, L. Feldman, R. Haglund, *J. Appl. Phys.* **2002**, *92*, 4031.
[49] J. Suh, R. Lopez, L. Feldman, R. Haglund, *J. Appl. Phys.* **2004**, *96*, 1209.

[50] S. Pauli, R. Herger, P. Willmott, E. Donev, J. Suh, R. Haglund, *J. Appl. Phys.* **2007**, *102*, 073527.
[51] A. Delabie, J. Swerts, S. V. Elshocht, S. H. Jung, P. I. Raisanen, M. E. Givens, E. J. Shero, J. Peeters, V. Machkaoutsan, J. W. Maes, *J. Electrochem. Soc.* **2011**, *158*, D259.
[52] H. C. M. Knoops, J. W. Elam, J. A. Libera, W. M. M. Kessels, *Chem. Mater.* **2011**, *23*, 2381.
[53] D. Céolin, J. M. Ablett, D. Prieur, T. Moreno, J.-P. Rueff, B. Pilette, T. Marchenko, L. Journel, T. Marin, R. Guillemin, M. Simon, *J. Electron Spectrosc. Relat. Phenom.* **2013**, *190*, 188.
[54] J. Mendialdua, R. Casanova, Y. Barbaux, *J. Electron. Spectrosc. Relat. Phenom.* **1995**, *71*, 249.
[55] M. Demeter, M. Neumann, W. Reichelt, *Surf. Sci.* **2000**, *41*, 454.
[56] K. Knapas, M. Ritala, *Crit. Rev. Solid State Mater. Sci.* **2013**, *38*, 167.
[57] F. de Groot, *Coord. Chem. Rev.* **2005**, *249*, 31.
[58] J. Wong, F. W. Lytle, R. P. Messmer, D. H. Maylotte, *Phys. Rev. B* **1984**, *30*, 5596.
[59] P. Chaurand, J. Rose, V. Briois, M. Salome, O. Proux, V. Nassif, L. Olivi, J. Susini, J.-L. Hazemann, J.-Y. Bottero, *J. Phys. Chem. B* **2007**, *111*, 5101.
[60] N. F. Mott, *Phil. Mag.* **1969**, *19*, 835.
[61] C. Neugebauer, M. Webb, *J. Appl. Phys.* **1962**, *33*, 74.